CONF-890820--5

ACCELERATED AGING EMBRITTLEMENT OF CAST DUPLEX STAINLESS STEEL - ACTIVATION ENERGY FOR EXTRAPOLATION*

H. M. Chung and O. K. Chopra

Materials and Components Technology Division
Argonne National Laboratory
Argonne, IL 60439

CONF-890820--5

DE90 001773

May 1989

To be submitted for presentation at the Fourth International Symposium on Environmental Degradation of Materials in Nuclear Power Systems - Water Reactors, August 6-10, 1989, Jekyll Island, GA.

*Work supported by the Office of Nuclear Regulatory Research, U. S. Nuclear Regulatory Commission.

ACCELERATED AGING EMBRITTLEMENT OF CAST DUPLEX STAINLESS STEEL - ACTIVATION ENERGY FOR EXTRAPOLATION

H. M. Chung and O. K. Chopra

Materials and Components Technology Division
Argonne National Laboratory
Argonne, IL 60439

ABSTRACT

Cast duplex stainless steels, used extensively in LWR systems for primary pressure boundary components such as primary coolant pipes, valves, and pumps, are susceptible to thermal aging embrittlement at reactor operating or higher temperatures. Since a realistic aging embrittlement for end-of-life or life-extension conditions (i.e., 32-50 yr of aging at 280-320°C) cannot be produced, it is customary to simulate the metallurgical structure by accelerated aging at ~400°C. Over the past several years, extensive data on accelerated aging have been reported from a number of laboratories. The most important information from these studies is the activation energy, namely, the temperature dependence of the aging kinetics between 280 and 400°C, which is used to extrapolate the aging characteristics to reactor operating conditions. The activation energies (in the range of 18-50 kcal/mole) are, in general, sensitive to material grade, chemical composition, and fabrication process, and a few empirical correlations, obtained as a function of bulk chemical composition, have been reported.

In this paper, a mechanistic understanding of the activation energy is described on the basis of the results of microstructural characterization of various heats of CF-3, -8, and -8M grades that were used in aging studies at different laboratories. The primary mechanism of aging embrittlement at temperatures between 280 and 400°C is the spinodal decomposition of the ferrite phase, and $M_{23}C_6$ carbide precipitation on the ferrite/austenite boundaries is the secondary mechanism for high-carbon CF-8 grade. However, the spinodal decomposition is accompanied by the simultaneous precipitation of the Si- and Ni-rich G-phase, which can influence the aging process. The precipitation characteristics of the G-phase have been quantitatively determined by dark-field TEM imaging, and the volume fraction of G-phase for the various heats has been measured. When the activation energies (ranging from 18 to 50 kcal/mole) were plotted as a function of the volume fraction of G-phase produced during accelerated aging, a good correlation was obtained regardless of variations in grade, bulk chemical composition, and fabrication process. This observation suggests that significant precipitation of G-phase appears to slow the kinetics of spinodal decomposition.

INTRODUCTION

Cast duplex stainless steels, used extensively in LWR systems for primary pressure boundary components such as primary coolant pipes, valves, and pumps, are susceptible to thermal aging embrittlement at reactor operating or higher temperatures. Since a realistic aging embrittlement for end-of-life or life-extension conditions (i.e., 32-50 yr of aging at 280-320°C) cannot be produced, it is customary to simulate the metallurgical structure by accelerated aging at ~400°C. Over the past several years, extensive data on accelerated aging have been reported from a number of laboratories.[1-4] The most important information from these studies is the "activation energy," namely, the temperature dependence of the aging kinetics between 280 and 400°C, which is used to extrapolate the aging characteristics to reactor operating conditions.

In the earlier investigations, embrittlement of the aged austenitic-ferritic stainless steels has been simply attributed to the precipitation of the Cr-rich α' phase in ferrite, a mechanism essentially identical to the "475°C embrittlement" of ferritic stainless steels.[1,2,5] According to this mechanism, an activation energy of aging similar to the activation energy of Cr diffusion in the ferrite phase (i.e., ~50 kcal/mole, or ~210 J/mole) would be expected. However, despite these common expectations, results of the extensive impact tests by Trautwein and Gysel showed invariably low activation energies (18-24 kcal/mole) for their heats of CF-3, -8, and -8M grades.[1] This was a surprising contrast to the high activation energies (~50 kcal/mole) observed and reported for ferritic stainless steels or for Cu-containing modified CF-8M stainless steels in the earlier investigations of Solomon and Devine.[5,6] In subsequent investigations, low, medium, and high activation energies ranging from 18 to 55 kcal/mole have been reported for heats of CF-3, -8, and -8M grades,[2-4] further compounding the complexities. In the

analysis of possible aging mechanisms and concomitant temperature dependence of the aging kinetics, Solomon and Devine[6] reviewed the possible role of the rate-controlling diffusion of interstitial elements (such as C and N) and the role of the grain-boundary segregation and precipitation to rationalize the results of Trautwein and Gysel.[1] However, the seemingly inconsistent behavior of the activation energy appears to remain essentially unexplained and a mechanistic understanding is yet to be provided. Besides these attempts on the mechanistic understanding, a few empirical correlations of the activation energy have been obtained as a function of the bulk chemical composition of the duplex material and have been reported in recent investigations.[2,4]

In the present study, aged specimens of the CF-3, -8, and -8M grades have been obtained from a number of laboratories and characterized by advanced metallographic techniques after impact tests and activation energy measurements. The activation energy, ranging from 18 to 55 kcal/mole, has then been correlated with the microstructural characteristics of the heats that represent a wide range of chemical composition, ferrite content, and fabrication procedures. The microstructure-activation energy correlation was then rationalized on the basis of a mechanistic model of aging embrittlement, eventually to provide insight for developing a better methodology for evaluating the long-term integrity of the cast stainless steel components.

EXPERIMENTAL

Laboratory-aged Specimens

Numerous laboratory-aged, broken Charpy specimens of CF-3, -8-, and -8M-grade stainless steel were obtained for examination from two laboratories.[1,4]

Aging was conducted at 400-280°C. The chemical composition and ferrite content of the laboratory-aged specimens are given in Table 1.

Microstructural Characterization

Details of the microstructural characterization of the aged specimens by transmission electron microscopy (TEM) and small-angle neutron scattering (SANS) have been reported elsewhere.[7,8] Some of the specimens, including reactor-aged specimens obtained from some decomissioned BWR and PWR, have been characterized by field-ion atom probe (FIAP) at Oxford University in England[9] and the University of Pittsburgh.[10,11]

Activation Energy from Literature Data

The "activation energy" of aging, i.e., the temperature dependence of the aging kinetics, was obtained from published data on room temperature Charpy-impact energy vs. aging time at 400 and 300°C[1] or 400 and 320°C.[4] Careful examination of the low-temperature impact data indicated a significant amount of uncertainty in some heats, and resulted in activation energies somewhat different from the literature, e.g., Heats No. 281 and 282[1] and Heat No. 47.[4]

RESULTS AND DISCUSSION

Mechanisms of Aging Embrittlement

In a number of previous reports, several metallurgical processes have been identified in association with thermal aging embrittlement of CF-3-, -8-, and -8M-grade cast stainless steels for the temperature range of 400-280°C. Five processes have been identified in ferrite phase, i.e., spinodal decompositin, nucleation and growth of platelike α', G-phase, γ_2 (austenite), and spherical $M_{23}C_6$.[8,12]

Two processes have been identified for the ferrite-austenite boundaries, i.e., $M_{23}C_6$ and Cr_2N precipitation.[12] Two processes have been identified in austenite of some of the aged specimens, i.e., spinodal-like decomposition[13] (involving Fe and Ni segregation) and sigma-phase precipitation on stacking faults and slip bands.[14] Occurrence of each process was strongly influenced by the chemical composition, ferrite content, aging conditions, and, to some extent, on the fabrication process. However, the spinodal decomposition of the ferrite occurred for aging at 400-280°C for all the specimens listed in Table 1.

Out of these processes, the primary mechanism of aging embrittlement was shown to be the spinodal decomposition of ferrite, which involves Fe, Cr, Ni segregation on a very fine scale of several atomic distances.[8] For high-carbon CF-8 or -8A (but not the Mo-containing CF-8M) materials, $M_{23}C_6$ carbide precipitation on the ferrite-austenite boundaries appears to be secondary embrittlement mechanism, since the phase boundary separation was evident in high proportion on the fracture surfaces of the aged specimens that contain significant amounts of the boundary $M_{23}C_6$.[15] These mechanisms of embrittlement have also been verified for reactor-aged specimens that were obtained from the decommissioned Shippingport PWR components (Fig. 1).[14]

A Model of Activation Energy

Since the spinodal decomposition of ferrite is the predominant mechanism of aging, understanding the effects of the aging temperature and ferrite chemical composition on the kinetics of the spinodal decomposition appear to be crucial to understand the complex behavior of the activation energy. However, the spinodal decomposition is accompanied by a simultaneous precipitation of the Si– and Ni-rich G-phase, which appears to influence the aging kinetics in a synergistic

manner.[8] The G-phase precipitation is, under otherwise identical conditions, faster at 400°C but is negligible for 300°C aging. Thus, the synergistic effect of the G-phase nucleation and precipitation appears to be pronounced for accelerated aging at 400°C but not for 300°C. Consequently, it is proposed that the activation energy of embrittlement (i.e., the relative kinetics of embrittlement during aging at 400 and 300°C) will be strongly influenced by the G-phase (or Ni-Si clustering) behavior at 400°C. A comparison of the FIAP profiles shown in Figs. 1A, 1B, and 1C reveals important information on the decomposition kinetics. Although the three ferrite grains for FIAP analysis were obtained from a single piece of specimen (MA9)[14], chemical composition was somewhat different (Table 2). A major difference is the Ni content, i.e., 9.70, 9.85, and 8.36 at. %, for the three grains. The low-Ni grain MA9-3 (Fig. 1C) showed a relatively less advanced spinodal decomposition than the other two grains. For example, compared to the maximum Cr fluctuation of ~45 at. % observed for the higher Ni grains, the low-Ni MA9-3 showed a maximum Cr fluctuation of ~37 at. %. The fact that neither G-phase nor Ni-Si clustering was observed[14] suggests that, under otherwise identical conditions, the lower Ni level in the ferrite matrix produces a slower spinodal decomposition.

From the above observation concerning the role of higher Ni content in accelerating the spinodal decomposition, as well as from the evidence that higher Ni content plays a similar role in α' nucleation and growth,[8,16] it can be deduced that the kinetics of the spinodal decomposition are influenced by the synergistic effect of G-phase nucleation and precipitation. Since the nucleation and precipitation of the Ni-rich G-phase will deplete the ferrite matrix of Ni, or because Ni-Si (or Ni-Si-Mo) clustering may occur prior to a G-phase nucleation and precipitation, spinodal decomposition will be slower for materials and aging conditions in

which the Ni-Si (or Ni-Si-Mo) clustering or G-phase precipitation is significant. This effect of retarding (under otherwise identical conditions) the decomposition is expected to be pronounced for aging at ~400°C, in which the Ni-Si clustering or G-phase precipitation is fast; however, for ~300°C aging, the retarding effect is expected to be negligible. Consequently, the activation energy of aging will be significantly smaller than the activation energy of normal spinodal decomposition in Fe-Cr binary alloys (i.e., the activation energy of Cr diffusion); instead, it will be comparable to the activation energy of Cr diffusion minus an apparent activation energy that is proportional to the synergistic effect of the Ni-Si (or Ni-Si-Mo) clustering or G-phase precipitation. This is illustrated by the schematic diagram shown in Fig. 2. In the figure, spinodal decomposition without G-phase nucleation and precipitation is characterized by an activation energy of Q_S~50 kcal/mole. With Ni-Si clustering or G-phase nucleation and precipitation, it is characterized by an effective activation energy equal to Q_S-Q_G, where Q_G is an apparent activation energy that is proportional to the extent of the synergistic effect.

If a significant precipitation of other embrittling phases (e.g., carbide or nitride) occurs on a ferrite/austenite boundary, aging will be influenced more at 400°C than at 300°C. Thus, the activation energy will be further altered as illustrated schematically in Fig. 3. In this figure, comparative activation energies for three hypothetical cases of microstructural transformation are shown schematically, i.e., (A) spinodal decomposition only, (B) Ni-Si (or Ni-Si-Mo) clustering or G-phase nucleation and precipitation plus (A), and (C) significant $M_{23}C_6$ precipitation on ferrite/austenite boundary during aging plus (B). Under otherwise similar conditions, Case (B) is likely to occur for heats containing a relatively high level of Si, Ni, and Mo in the ferrite[7]. Case (C) is likely to occur for CF-8 or -8A

heats containing a high level of C, but not for CF-8M. According to this model, activation energy is expected to be a function of the ferrite chemical compositions that influence the G-phase and $M_{23}C_6$ precipitations.

Activation Energy-Microstructure Correlation

Since the spinodal decomposition occurs on a fine scale of several atomic distances, it is likely that the early-stage Ni-Si (or Ni-Si-Mo) clustering and G-phase nucleation will influence the kinetics of the decomposition, particularly for aging at 400°C. In fact, aging embrittlement at 400°C occurs during a relatively early period, when the G-phase precipitates or nuclei are too small to be resolved by TEM. However, a later stage of G-phase precipitation and Ostwald ripening[7] is expected to be a fair indication of the relative extent of the early-stage reactions. Therefore, G-phase volume fraction, determined for different heats after aging at the same temperature (e.g., 400°C) for the same time (e.g., 10,000 or 30,000 h), will provide an indication of the relative extent of the early-stage reactions.

For long-term aging at 400°C, G-phase volume fraction can be measured by dark-field TEM imaging. A number of heats were selected to conduct the dark-field imaging analysis. G-phase reflections could be identified readily for specimens in which the G-phase volume fraction is high, e..g, Heat Nos. P4 and 286 aged at 400°C for >10,000 h. For specimens with smaller volume fractions, the strong {333} reflections[7] of the G-phase could be identified by tilting the specimen orientation close to (110), (311), or (133) zone of the ferrite. In many cases, even the intensity of the {333} reflections was too weak to be visible on the selected area diffraction pattern. In such cases, the objective aperture was placed on a blind spot on which the {333} reflection is supposed to be located. A dark-field image

could be then successfully produced in many cases from the blind spot (e.g., Heat Nos. 60 and 51 aged at 400°C for 10,000 h). In other cases, images produced from a spot containing both the ferrite and G-phase reflections showed satisfactory results (e.g., Heat Nos. 59 and 292, aged at 400°C for 10,000 h). For each specimen for which the G-phase size and distribution have been analyzed, dark-field images were obtained from typically 7 to 10 different regions of 2 to 4 different ferrite grains. The 7 to 10 images were obtained from local ferrite regions from which the bright-field intensity of the electron beam was similar under the condition of constant condenser-aperture spread. In this way, ferrite regions of similar thickness could be examined. Out of such 7 to 10 images, an image representative of the G-phase distribution of the specimen was selected. Then, a stereopair of dark-field G-phase images were obtained from the same representative region after tilting the specimen by 5 to 10 degrees. Film thickness of the selected region was then determined by measuring the parallex with a Cartographic Engineering Ltd. mirror stereoscope. The local film thickness is given then by the equation

$$t = \frac{P}{2\,M\,\sin\theta}$$

where t = film thickness, P = parallex measured for G-phase particles located on top and bottom surfaces of the film, M = magnification of the image, and θ = specimen tilt angle.

In Fig. 4, results of TEM analysis of the G-phase size and distribution are given for eight different heats aged at 400°C for 30,000 h and one heat aged at 400°C for 70,000 h. For each heat, the activation energy determined from room-temperature impact tests is given. It seems from examination of Fig. 4 that a monotonic correlation between the G-phase volume fraction and the activation

energy is evident, i.e., the higher the volume fraction, the lower the energy. For high-carbon CF-8 Heat Nos. 56, 59, and 60, approximately 60% of the ferrite-austenite boundary was associated with $M_{23}C_6$ precipitates (Heat No. 56 in Fig. 4; and Heat Nos. 59 and 60 in Fig. 5). G-phase volume fraction was determined from Fig. 4 and the measured local film thickness, and the results were plotted against the activation energy in Fig. 6 for f_c ~0.0 and f_c ~0.6, where f_c is the fraction of the ferrite-austenite boundary covered by the $M_{23}C_6$ carbide. Also included in the figure are similar data obtained for a number of heats that were tested by GE[5] and CEGB[3] and whose microstructural characterization was reported to contain no or negligible amount of G-phase. For aging at 400°C for 10,000 h, the microstructural characteristics similar to Fig. 4 and a correlation similar to Fig. 6 is shown in Figs. 7 and 8, respectively.

The correlations shown in Figs. 6 and 8 indicate that the mechanistic model of activation energy, illustrated schematically in Fig. 3, is essentially valid. For heats containing an insignificant amount of boundary $M_{23}C_6$, a high activation energy was associated with a negligible amount of G-phase precipitates (e.g., Heat No. 51), and, in contrast, a low activation energy was associated with a significant amount of G-phase (e.g., Heat No. P4). In general, CF-8M grade materials, containing Mo and a relatively high level of Ni, showed more extensive G-phase precipitation but a smaller amount of the boundary $M_{23}C_6$. Thus, the activation energy of a CF-8M heat tends to be low. However, the characteristics of G-phase precipitation were complex and, in general, it was difficult to predict the behavior solely on the basis of bulk chemical composition.

Absolute Rate of Aging

In contrast to the activation energy of aging (i.e., manifesting the relative rate of aging at temperatures of 400 and 300°C), it was difficult to establish a correlation between the absolute rate of aging (e.g., for 400°C) and microstructural characteristics. This seems to be caused primarily by the complexities of the kinetics of the spinodal decomposition and G-phase precipitation, which are influenced by many other factors (besides the Ni effect) e.g., ferrite content, morphology, and ferrite chemical compositions. Given a similar overall chemical composition, the ferrite chemical composition is expected to be influenced by the fabrication process. The absolute rates of aging of the heats included in the above analysis have been plotted in Figs. 9 for comparison. In Fig. 9A, schematic aging kinetics at 400 and 300°C are shown in which the characteristic time to reach the mid-level impact energy is defined for the two temperatures. The characteristic aging times t_{400} and t_{300} are convenient parameters that represent the absolute rates of aging at the two temperatures. In Fig. 9B, the characteristic aging times have been plotted as a function of the inverse temperature for CF-3, -8, and -8M heats that have been aged in a number of laboratories (i.e., GE, G. Fischer, Framatome, CEGB, and ANL). The figure shows that the scatter in the absolute rate of aging is similar for the two aging temperatures. The slope of line for each heat produces an activation energy. In the figure, CF-3, -8, and -8M grades have been denoted by different symbols.

As pointed out previously, most of the G. Fischer (GF) heats[1] shown in Fig. 9B exhibit an activation energy that is invariably low. The distinct aging behavior of the GF materials may be associated with a number of factors, i.e., fabrication process, additional solution anneal at 1010°C, relatively low Ni and C, and relatively high Si levels. The high level of Si in most of the GF materials promotes

more extensive G-phase precipitation, and, as shown in Figs. 6 and 8, this is conducive to a lower activation energy. However, two of the GF heats, i.e., Heat Nos. 281 and 282, contain very low Si (0.45 and 0.35 wt %, respectively, Table 1). Impact energies measured for these two heats show that the kinetics of 300°C aging are relatively slower than those for other heats. This is shown in Fig. 9B. The low-Si heats (Nos. 281 and 282) show activation energies of 33 and 48 kcal/mole, respectively. This is in contrast to the behavior of the rest of the high-Si GF heats, which invariably showed low activation energies (18-24 kcal). Since the low Si levels of Heat Nos. 281 and 282 are expected to produce less Ni-Si clustering or G-phase precipitation, the observation tends to provide further support for the validity of the mechanistic model.

Effect of Fabrication Process

The morphology of G-phase precipitates in Figs. 4 and 7 reveal some important characteristics. That is, in contrast to most of the GF heats, some of the ANL heats contained a high density of dislocations in the ferrite phase. G-phase precipitation occurred preferentially on the dislocations in some of the ANL heats, e.g., Heat Nos. 64, 65, 63, and 47. This behavior indicates that the activation energy is influenced by dislocation structures, since dislocations promote G-phase nucleation and precipitation. The dislocations in the ferrite apparently are produced during the fabrication process because of mechanical and thermal stresses. Dislocations produced during an impact test will not accompany the G-phase precipitates. Thus, it seems that the fabrication process is an important consideration in evaluating the activation energy of aging.

Another aspect of the fabrication process that may influence the activation energy is the variation in the actual chemical composition of ferrite rather than

the bulk composition of the steel. An example of this is given in Table 2 where the variation in Ni content among the nominally identical FIAP tip specimens apparently alters the kinetics of spinodal decomposition (Fig. 1). Ni and Fe atoms are, in general, partitioned preferentially in austenite, and, in contrast, Cr, Mo, and Si atoms are preferentially partitioned in ferrite. However, the degree of partitioning of those elements, known to influence the kinetics of the spinodal decomposition and G-phase precipitation, is expected to be significantly influenced by the fabrication process. Not much information has been reported in literature on the quantitative behavior of the partitioning. Ferrite composition data available from EDS and FIAP analyses have been collected and the ferrite partitioning ratio (i.e., ferrite-to-overall chemical composition ratio) has been calculated. The results are summarized in Table 3. Of particular interest in the table is the partitioning ratios of Ni, Si, Mo and Cr, which strongly influence the kinetics of the spinodal decomposition and G-phase precipitation, and hence, the activation energy. Although uncertainty limits of the EDS analysis, in particular for Si, should be considered unacceptable, the results in the table clearly indicate that the partitioning ratios for those elements are significantly influenced by the variation in the fabrication process.

In view of the above findings, it seems evident that not only the absolute rate of aging but also the activation energy are strongly influenced by the fabrication process. The relationships among the bulk composition, critical factors of fabrication process, microstructure, and the activation energy of aging are illustrated schematically in Fig. 10.

CONCLUSIONS

1. Kinetics of the spinodal decomposition (i.e., the primary mechanism of the aging embrittlement) and G-phase precipitation are strongly influenced by nominally small differences in fabrication process and ferrite chemical composition, in particular, Ni, Mo, Si, and C. Higher level of Ni in ferrite matrix appears to accelerate the spinodal decomposition under otherwise identical conditions. The decomposition rate also appears to be influenced strongly by Ni-Si (or Ni-Si-Mo) clustering or nucleation and growth of G-phase.

2. It may be difficult to obtain a single empirical correlation of activation energy as a function bulk composition that can provide a reliable extrapolation of aging behavior regardless of fabrication process and thermomechanical history. However, a mechanistic correlation based on microstructural characteristics (i.e., G-phase volume fraction in ferrite and $M_{23}C_6$ distribution on ferrite-austenite boundaries) was obtained, and it was shown that this correlation provides a good explanation of the complex behavior of activation energy regardless of grade, fabrication process, and thermomechanical history.

ACKNOWLEDGMENTS

This work was supported by the Office of Nuclear Regulatory Research, U. S. Nucledar Regulatory Commission. The author is grateful to A. Trautwein of the Georg Fischer Co. of Switzerland for his efforts in making the specimens from long-term-aged laboratory heats available for this work, and to R. A. Conner, Jr. and A. Philippides for their contributions to the experimental effort. The author is also grateful to T. R. Leax of the Westinghouse Electric Corporation for the FIAP analysis of the Shippingport reactor specimens. The author also wishes to

thank J. Muscara, E. Woolridge, W. J. Shack, and T. F. Kassner for helpful discussions.

REFERENCES

1. A. Trautwein and W. Gysel, "Influence of Long Time Aging of CF-8 and CF-8M Cast Steel at Temperatures between 300 and 500°C on the Impact Toughness and the Structure Properties," Stainless Steel Castings, Behal, V. G. and Melilli, A. S., Eds., ASTM STP 756, Philadelphia, PA, 1982, p. 165.

2. G. Slama, P. Petrequin, and T. Mager, "Effect of Aging on Mechanical Properties of Austenitic Stainless Steel Castings and Welds," presented at SMIRT Post-Conference Seminar 6, Assuring Structural Integrity of Steel Reactor Pressure Boundary Components, August 29-30, 1983, Monterey, CA.

3. K. N. Akhurst and P. H. Pumphrey, "The Aging Kinetics of CF-3 Cast Stainless Steel in the Temperature Range 300°C to 400°C," RO/L/3354/R88, November 1988, Central Electricity Generating Board Research Laboratories, United Kingdom.

4. O. K. Chopra and H. M. Chung, "Aging Degradation of Cast Stainless Steels: Effects on Mechanical Properties," in Proc. 3rd Int. Symposium on Environmental Degradation of Materials in Nuclear Power Systems-Water Reactors, August 30-September 3, 1987, Traverse City, MI, Theus, G. J. and Weeks, J. R., eds., The Metallurgical Society, 1988, pp. 737-748.

5. H. D. Solomon, "Investigation of the Physical Metallurgy, Mechanical Properties, and Embrittlement of Alloy U50," Report 76CRD188, April 1977, General Electric Co., Schenectady, NY.

6. H. D. Solomon and T. M. Devine, Jr., "Duplex Stainless Steels - A Tale of Two Phases," Report 82CRD276, November 1982, General Electric Co., Schenectady, NY.

7. H. M. Chung and O. K. Chopra, "Characterization of Duplex Stainless Steels by TEM, SANS, and APFIM Techniques," in Proc. Intl. Metallographic Symp. Characterization of Advanced Materials, Monterey, CA, July 27-29, 1987.

8. H. M. Chung and O. K. Chopra, "Kinetics and Mechanism of Thermal Aging Embrittlement of Duplex Stainless Steels," Proc. Third International Symposium on Environmental Degradation of Materials in Nuclear Power Systems–Water Reactors, August 30-September 3, 1987, Traverse City, MI, G. J. Theus and J. R. Weeks, eds., The Metallurgical Society, 1988, pp. 359-370.

9. T. J. Godfrey, and G. D. W. Smith, "The Atom Probe Analysis of a Cast Duplex Stainless Steel," Proc. 33rd International Field Emission Symposium, July 7-11, 1986, West Berlin, Germany.

10. T. R. Leax, Westinghouse Electric Corp., 1988, unpublished work.

11. O. K. Chopra and H. M. Chung, Long-Term Embrittlement of Cast Duplex Stainless Steels in LWR Systems: Semiannual Report, October 1987-March 1988, NUREG/CR-4744, Vol. 2, No. 3, ANL-89-36, Argonne National Laboratory.

12. O. K. Chopra and H. M. Chung, Long-Term Embrittlement of Cast Duplex Stainless Steels in LWR Systems: Semiannual Report, April-September 1987, NUREG/CR-4744, Vol. 2, No. 2, ANL-89-6, Argonne National Laboratory.

13. H. M. Chung, "Spinodal–Like Decomposition of Austenite in Long-Term-Aged Duplex Stainless Steel," paper presented at the Metallurgical Society Annual Meeting, February 27-March 3, 1989, Las Vegas, NV.

14. H. M. Chung, "Thermal Aging of Some Decommissioned Reactor Cast Stainless Steel Components and Methodology for Life Prediction," Paper submitted to ASME-Material Properties Council Symposium on Plant Life Extension for Nuclear Components, July 24-27, 1989, Honolulu, Hawaii.

15. H. M. Chung and O. K. Chopra, "Microstructure of Cast Duplex Stainless Steel after Long-Term Aging," in Proc. Second Intl. Symp. on Environmental Degradation of Materials in Nuclear Power Systems - Water Reactors, September 9-12, 1985, Monterey, CA, American Nuclear Society, LaGrange Park, IL, pp. 287-292 (1986).

16.. H. D. Solomon and L. M. Levinson, "Mössbauer Effect Study of '475°C Embrittlement' of Duplex and Ferritic Stainless Steels," Acta Met. 26, 429-442 (1978).

17. W. H. Bamford, F. J. Witt, and S. A. Swamy, "Aging Effects on Cast Stainless Steels," in Properties of Stainless Steels in Elevated Temperature Service, ed. M. Prager, MPC-Vol. 26, PVP-Vol. 132, American Society for Mechanical Engineers, 1987, pp. 49-63.

18. M. K. Miller and J. Bentley, "Characterization of Fine-Scale Microstructures in Aged Primary Coolant Pipe Steels," in Proc. 3rd International Symposium on Environmental Degradation of Materials in Nuclear Power Systems-Water Reactors, August 30-September 3, 1987, Traverse City, MI, G. J. Theus and J. R. Weeks, eds., The Metallurgical Society, 1988, pp. 341-349.

19. T. F. Leax, Westinghouse Electric Corporation, unpublished work, 1989.

20. T. R. Leax, S. S. Brenner, and J. A. Spitznagel, "Atom Probe Analysis of Thermal Aging Effects on Cast Stainless Steel," Westinghouse Electric Corp., unpublished work, 1987.

Fig. 1. Results of FIAP and TEM Analyses of the Shippingport PWR Components Showing the Primary (Spinodal Decomposition) and Secondary ($M_{23}C_6$ Precipitation on Ferrite-Austenite Boundary) Processes of the Aging. (A)-(C) are the Fe and Cr profiles of three ferrite grains, respectively, MA9-1, -2, and -3 of a hot-leg main valve specimen (see Table 2 for ferrite chemical composition of each grain), and (D) is the $M_{23}C_6$ morphology of a cold-leg check valve of CF-8A grade.

Fig. 2. Schematic Illustration of Activation Energies for Spinodal Decomposition (Q_S ~48 kcal/mole) and G-Phase Precipitation (Q_G) in Ferrite. Effective activation energy from mechanical properties is expected to be comparable to Q_S-Q_G as shown when G-phase precipitation or Ni-Si clustering is significant.

Fig. 3. Schematic Illustration of Relative Kinetics and Activation Energies for Three Hypothetical Cases of Metallurgical Transformation under Otherwise Identical Conditions. (A) Spinodal decomposition only (in ferrite), (B) G-phase precipitation or Ni-Si clustering plus (A), (C) significant $M_{23}C_6$ precipitation on austenite/ferrite boundary during aging plus (B).

Fig. 4. Dark-Field TEM Morphologies of G-Phase Size and Distribution in Ferrite of Several Heats Observed after Aging at 400°C for 30,000 h. Heat GF-280 was aged for 70,000 h. Activation energy for each heat is given.

Fig. 5. $M_{23}C_6$ Carbide on Ferrite-Austenite Boundary for (A) Heat 59 and (B) Heat 60, both Observed after Aging at 400°C for 30,000 h.

Fig. 6. Activation Energy versus the Volume Fraction of G-Phase in Ferrite for Aging at 400°C for ≥30,000 h. f_c denotes fraction of the ferrite-austenite boundary covered by $M_{23}C_6$.

Fig. 7. Dark-Field Morphology of G-Phase after Aging at 400°C for 10,000 h. Activation energy for each heat is given.

Fig. 8. Activation Energy versus G-Phase Volume Fraction in Ferrite for Aging at 400°C for 10,000 h.

Fig. 9. Schematic Impact Energy versus Aging Time Showing Times for 50% Impact-Energy Drop for 400 and 300°C Aging (A), and Aging Times for 50% Impact-Energy Drop Observed for a Number of Heats of Various Grades of Stainless Steel (B).

Fig. 10. Schematic Illustration of the Influence of Fabrication Process and Microstructural Evolution on the Activation Energy of Aging. Effects of $M_{23}C_6$ precipitation are not included.

Table 1. Chemical Composition of Laboratory-Aged Heats of CF-3-, CF-8-, and CF-8M-Grade Duplex Stainless Steels used for Microstructural Characterization and Studies of the Kinetics and Mechanisms of Aging

Heat No.	Grade	Composition (wt.%)									Ferrite Content (%)
		Mn	Si	Mo	Cr	Ni	P	S	N	C	
280N	CF-8	0.50	1.37	0.25	21.60	8.00	0.015	0.006	0.029	0.028	38.0
280	CF-8	0.50	1.37	0.25	21.60	8.00	0.015	0.006	0.029	0.028	38.0
278	CF-8	0.28	1.00	0.13	20.20	8.27	0.008	0.019	0.027	0.038	15.0
281	CF-8	0.41	0.45	0.17	23.10	8.60	0.020	0.010	-	0.036	30.0
282	CF-8	0.43	0.35	0.15	22.50	8.53	0.020	0.019	-	0.035	38.0
292	CF-8	0.34	1.57	0.13	21.60	7.52	0.018	0.016	-	0.090	28.0
286	CF-8M	0.40	1.33	2.44	20.20	9.13	0.044	0.015	0.063	0.072	22.0
47	CF-3	0.60	1.06	0.59	19.81	10.63	-	-	0.028	0.018	16.3
52	CF-3	0.57	0.92	0.35	19.49	9.40	-	-	0.052	0.009	13.5
51	CF-3	0.63	0.86	0.32	20.13	9.06	-	-	0.058	0.010	18.0
60	CF-8	0.67	0.95	0.31	21.05	8.34	-	-	0.058	0.064	21.1
56	CF-8	0.57	1.05	0.34	19.65	9.28	-	-	0.030	0.066	10.1
59	CF-8	0.60	1.08	0.32	20.33	9.34	-	-	0.045	0.062	13.5
63	CF-8M	0.61	0.58	2.57	19.37	11.85	-	-	0.031	0.055	10.4
P4	CF-8M	1.07	1.02	2.05	19.64	10.00	-	-	0.151	0.040	10.4
64	CF-8M	0.60	0.63	2.46	20.76	9.40	-	-	0.038	0.038	28.4
65	CF-8M	0.50	0.48	2.57	20.78	9.63	-	-	0.064	0.049	23.4
74	CF-8M	0.54	0.73	2.51	19.11	9.03	-	-	0.048	0.064	18.4
75	CF-8M	0.53	0.67	2.58	20.86	9.12	-	-	0.052	0.065	27.8

Table 2. Summary of Chemical Composition Analysis of Three Ferrite Grains of a Shippingport PWR Hot–Leg Main Valve Specimen[14] by Field Ion Atom Probe[(a)]

Grain Number	Total Number of Ions Analyzed	Ferrite Composition (at.%)						
		Fe	Cr	Ni	Mo	Si	Mn	P
MA9–1	31,737	66.32	21.01	9.70	0.69	0.63	1.48	0.16
MA9–2	76,819	65.92	21.61	9.85	0.65	0.67	1.08	0.21
MA9–3	62,713	65.86	22.97	8.36	0.65	0.67	1.22	0.27

[(a)]See Figs. 1(A) to (C) for the atom–probe data.

Table 3. Summary of Ferrite-to-Overall Chemical Composition Ratios (Ferrite Partitioning Ratio) of Aged Cast Duplex Stainless Steel

Heat Number or Component	Grade	Aging[a] Conducted at	Temperature (°C)	Aging Time (h)	Ferrite Content (%)	Specimen Number	Ferrite/Bulk Partitioning Ratio							Analysis[b] Technique	Reference[c]
							Fe	Cr	Ni	Mo	Si	Mn	P		
L	CF-8M	FRA	400	7,500	17.5	L-01	0.95	1.29	0.60	1.64	1.91	-	-	EDS	17
						L-02	0.95	1.27	0.57	1.66	2.53	-	-	EDS	17
						L-03	0.94	1.28	0.60	1.92	1.23	1.01	-	EDS	18
278	CF-8	GF	400	70,000	15.0	278-A	0.94	1.41	0.45	2.77	1.42	0.28	-	EDS	18
Hot-Leg Main Valve	CF-8	Shippingport PWR	Reactor	~22 yr	10.0	MAC-10	0.98	1.31	0.54	0.78	0.40	-	-	EDS	19
						MAC-10.99		0.95	0.98	4.92	1.34	2.052.19		FIAP	Table 2, this paper
						MAC-30.99		1.04	0.84	4.64	1.42	1.693.70		FIAP	
Pump Volute	CF-8	Shippingport PWR	Unaged	Unaged	16.2	VRC-10	0.98	1.24	0.64	-	0.96	-	-	EDS	19
Y4331	CF-8MC	FRA	400	700	20.0	4331-A	0.96	1.20	0.72	1.68	1.31	0.26	-	EDS	20
						4331-B	0.93	1.14	0.76	2.48	1.62	1.56	-	FIAP	20
Y3296	CF-8MC	FRA	400	8,000	33.0	3296-A	0.96	1.18	0.81	1.81	1.20	0.15	-	EDS	20
						3296-B	0.95	1.09	0.89	1.95	1.29	1.66	-	FIAP	20

[a]FRA = Framatome, GF = Georg Fischer Co.
[b]EDS = Energy-Dispersive X-ray Analysis, FIAP = Field-Ion Atom Probe.
[c]Source reference of EDS or FIAP analysis.

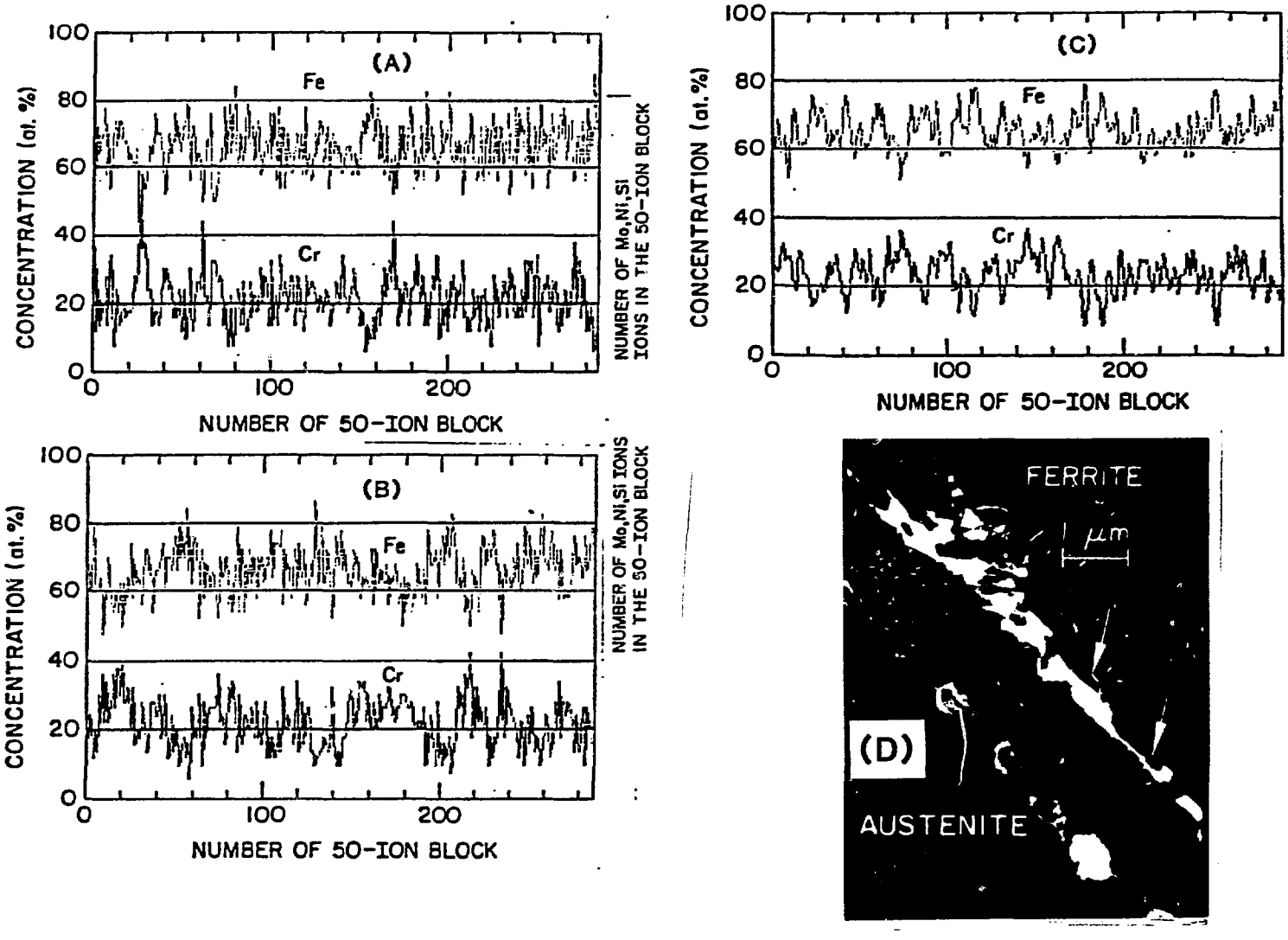

Fig. 1. Results of FIAP and TEM Analyses of the Shippingport PWR Components Showing the Primary (Spinodal Decomposition) and Secondary ($M_{23}C_6$ Precipitation on Ferrite-Austenite Boundary) Processes of the Aging. (A)-(C) are the Fe and Cr profiles of three ferrite grains, respectively, MA9-1, -2, and -3 of a hot-leg main valve specimen (see Table 2 for ferrite chemical composition of each grain), and (D) is the $M_{23}C_6$ morphology of a cold-leg check valve of CF-8A grade.

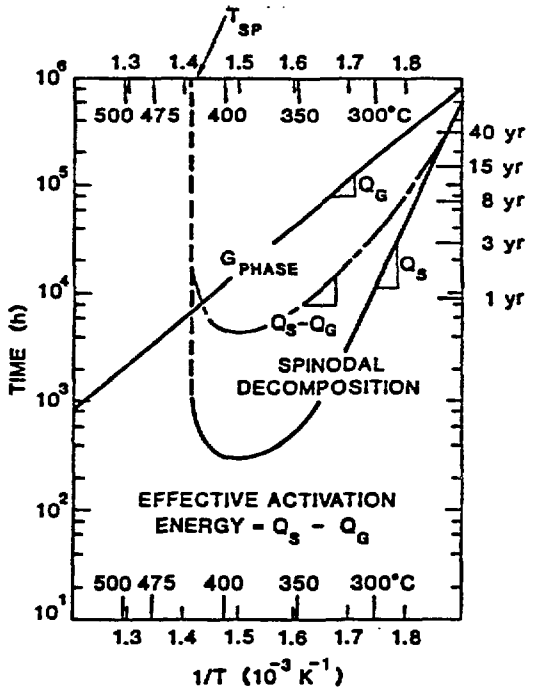

Fig. 2. Schematic Illustration of Activation Energies for Spinodal Decomposition (Q_S ~48 kcal/mole) and G-Phase Precipitation (Q_G) in Ferrite. Effective activation energy from mechanical properties is expected to be comparable to Q_S-Q_G as shown when G-phase precipitation or Ni-Si clustering is significant.

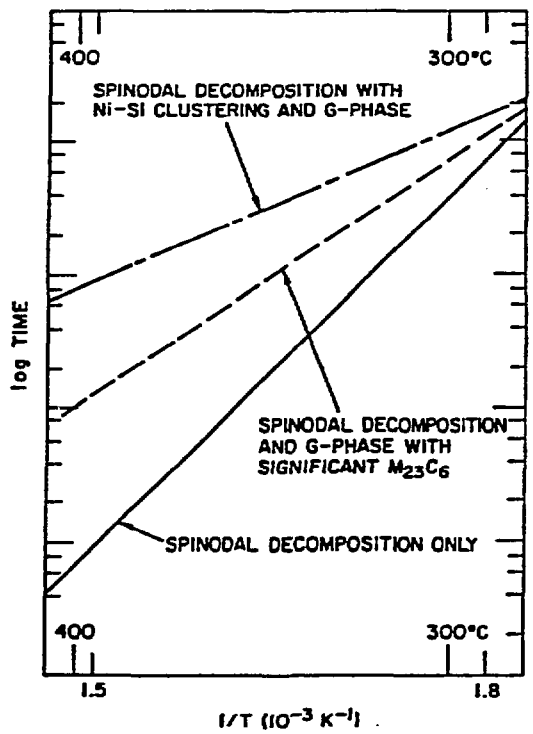

Fig. 3. Schematic Illustration of Relative Kinetics and Activation Energies for Three Hypothetical Cases of Metallurgical Transformation under Otherwise Identical Conditions. (A) Spinodal decomposition only (in ferrite), (B) G-phase precipitation or Ni-Si clustering plus (A), (C) significant $M_{23}C_6$ precipitation on austenite/ferrite boundary during aging plus (B).

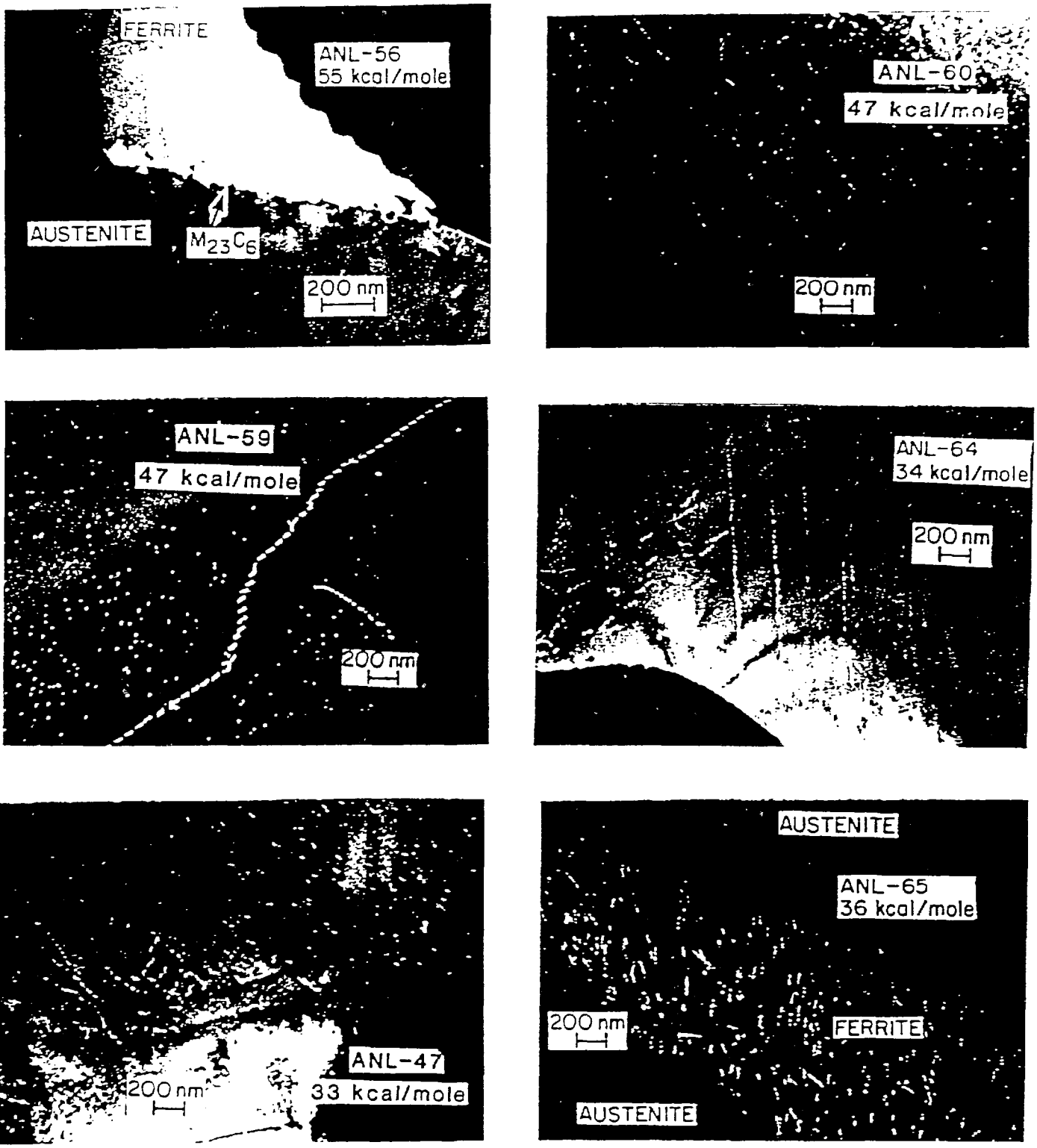

Fig. 4. Dark-Field TEM Morphologies of G-Phase Size and Distribution in Ferrite of Several Heats Observed after Aging at 400 C for 30,000 h. Heat GF-2s0 was aged for 70,000 h. Activation energy for each heat is given.

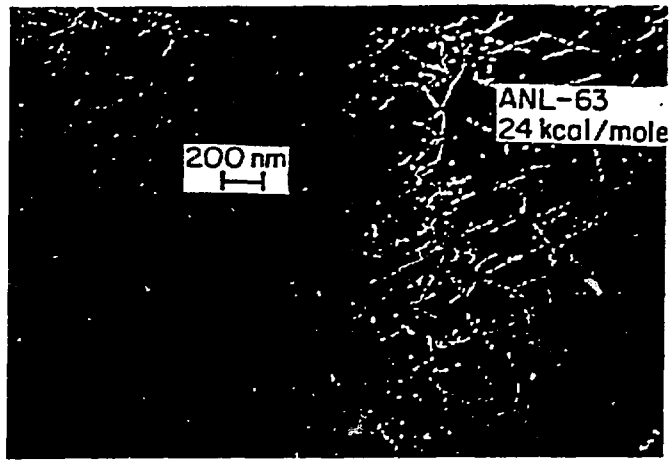
ANL-63
24 kcal/mole
200 nm

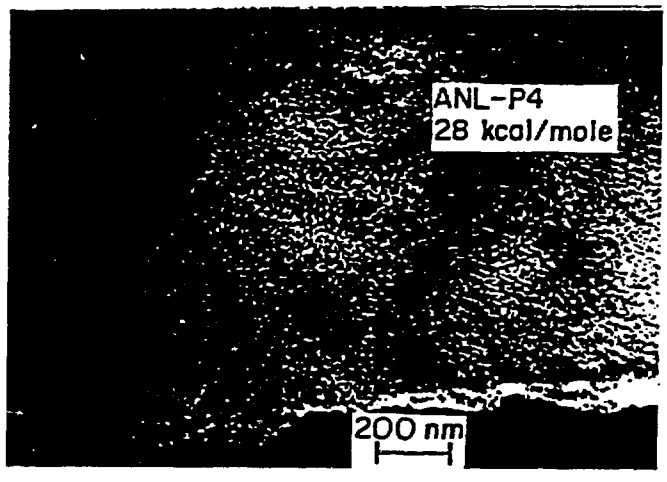
ANL-P4
28 kcal/mole
200 nm

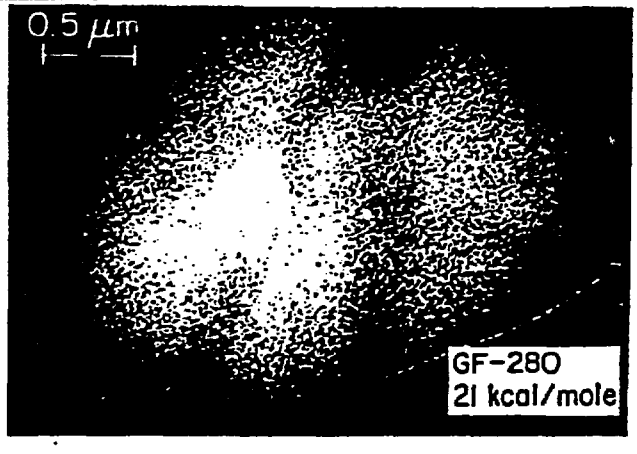
0.5 μm
GF-280
21 kcal/mole

Fig. 4 (Contd.)

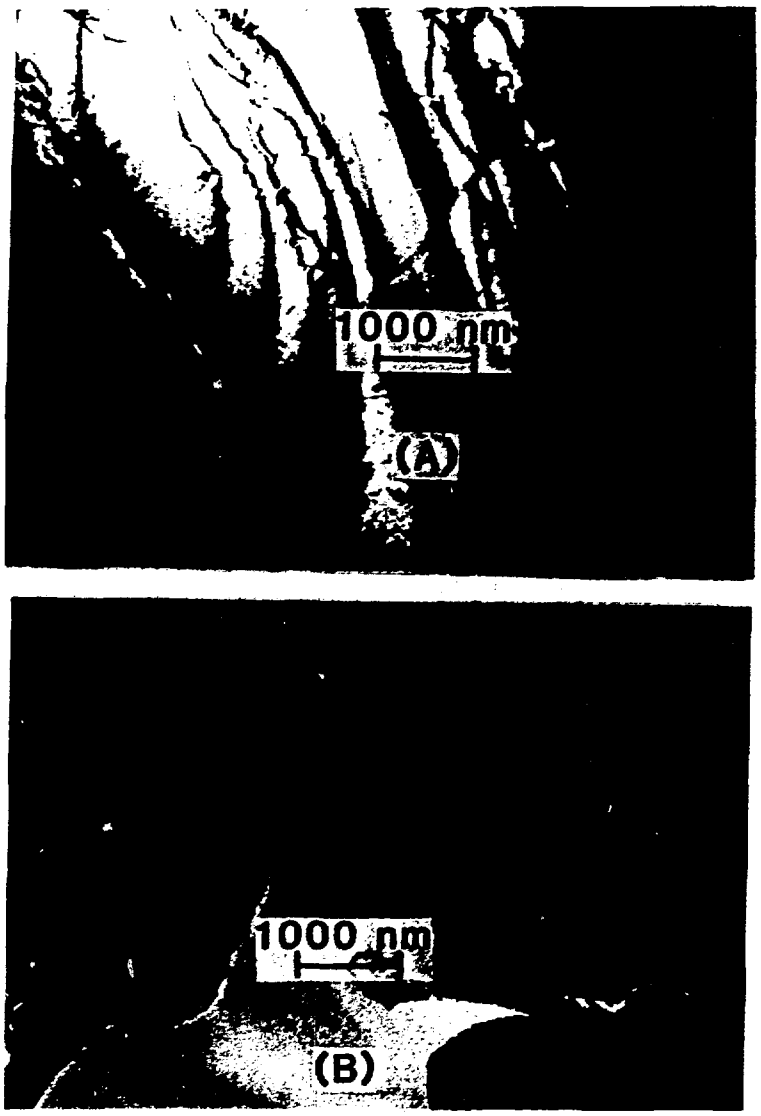

Fig. 5. $M_{23}C_6$ Carbide on Ferrite-Austenite Boundary for (A) Heat 59 and (B) Heat 60, both Observed after Aging at 400°C for 30,000 h.

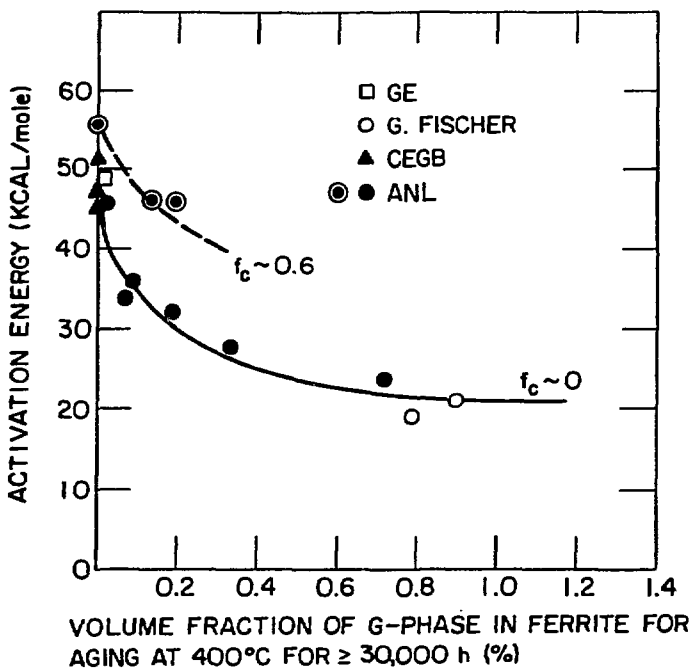

Fig. 6. Activation Energy versus the Volume Fraction of G-Phase in Ferrite for Aging at 400°C for ≥30,000 h. f_c denotes fraction of the ferrite-austenite boundary covered by $M_{23}C_6$.

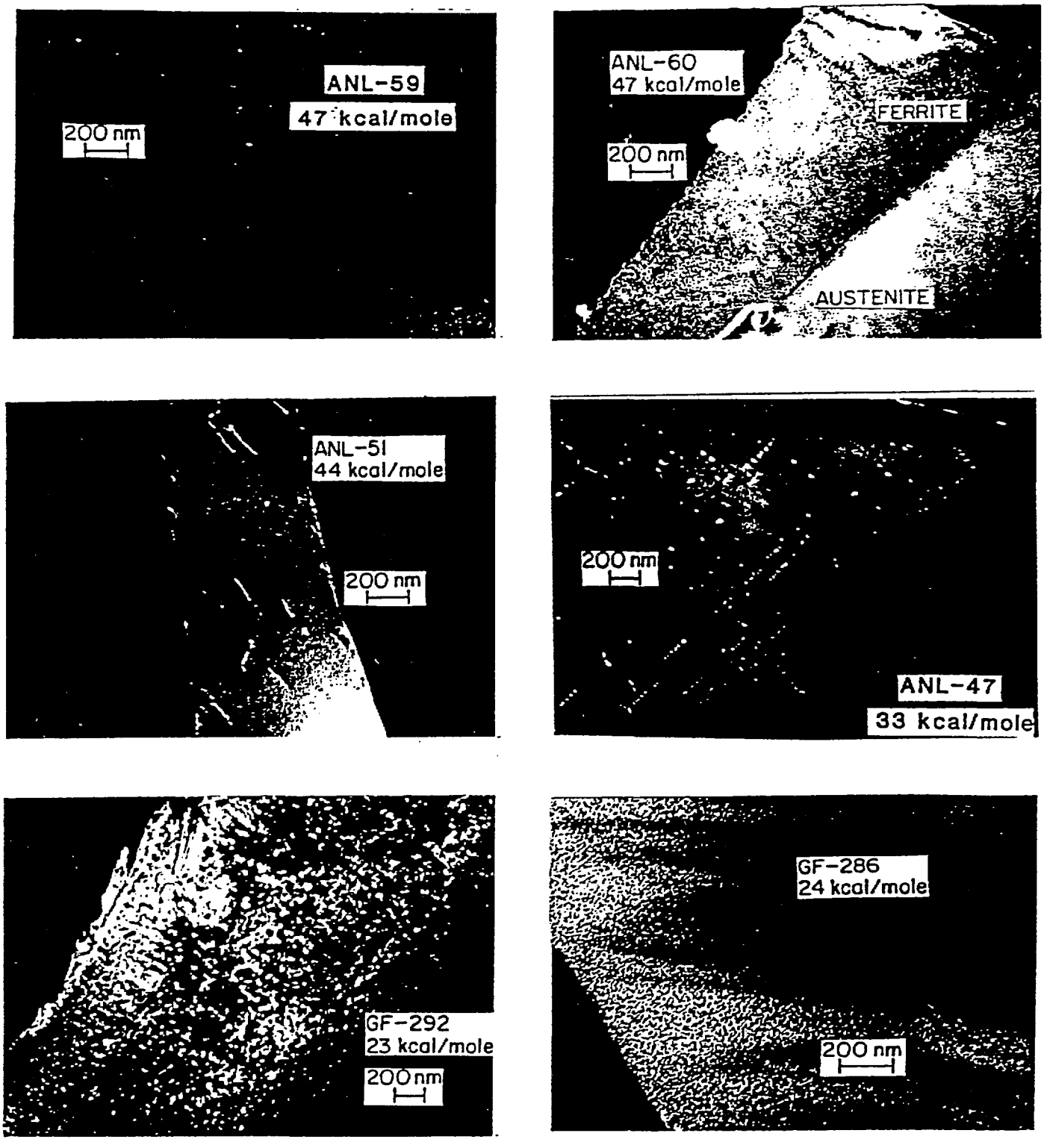

Fig. 7. Dark-Field Morphology of G-Phase after Aging at 400°C for 10,000 h. Activation energy for each heat is given.

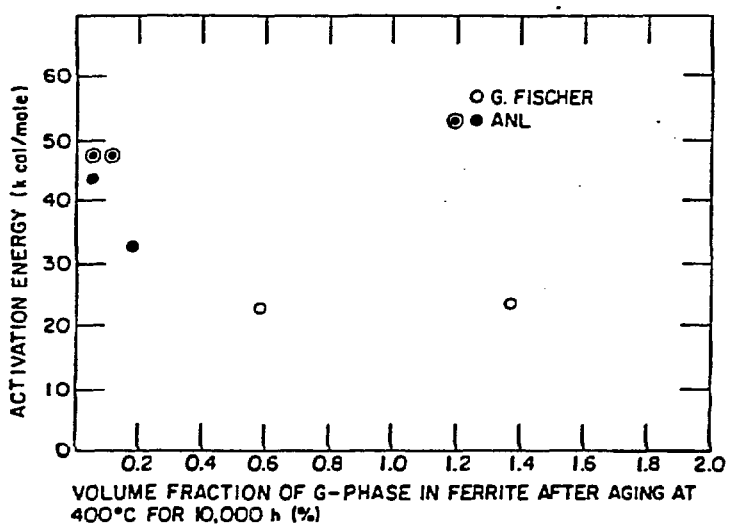

Fig. 8. Activation Energy versus G-Phase Volume Fraction in Ferrite for Aging at 400°C for 10,000 h.

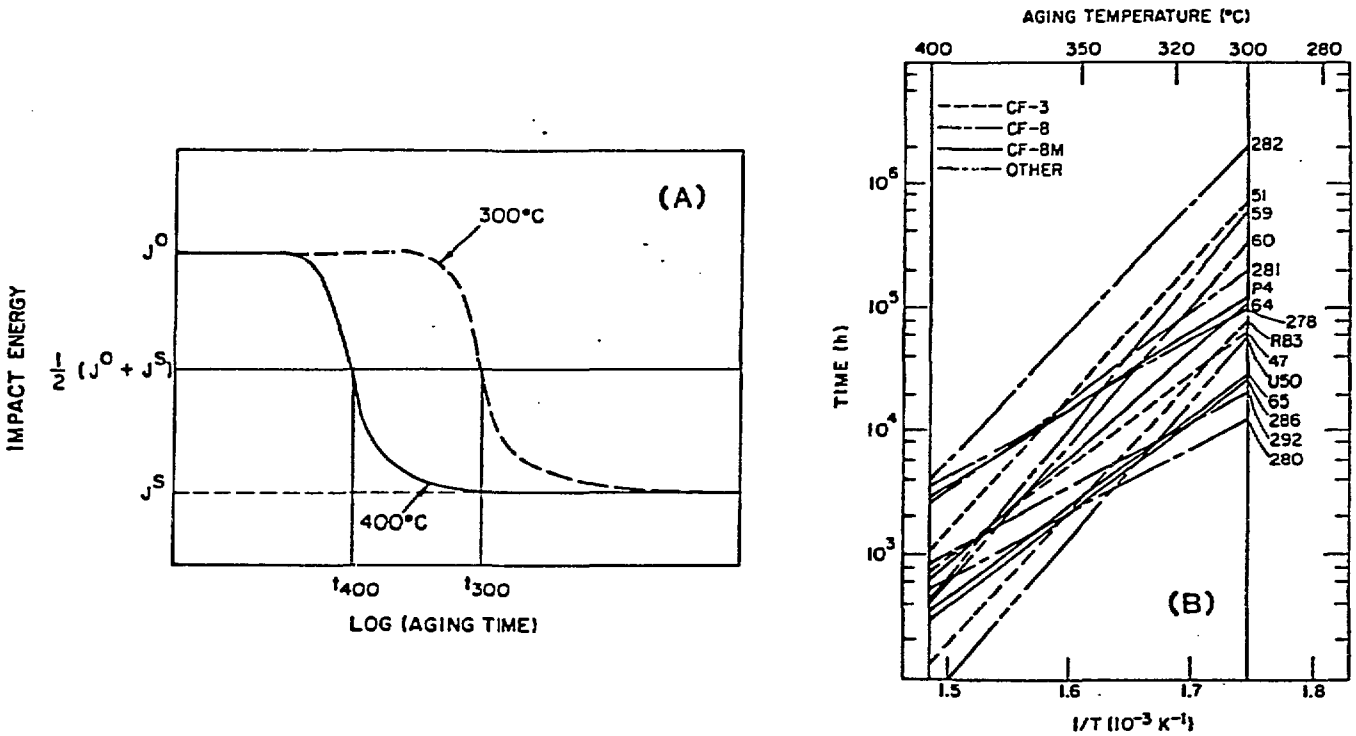

Fig. 9. Schematic Impact Energy versus Aging Time Showing Times for 50% Impact-Energy Drop for 400 and 300°C Aging (A), and Aging Times for 50% Impact-Energy Drop Observed for a Number of Heats of Various Grades of Stainless Steel (B).

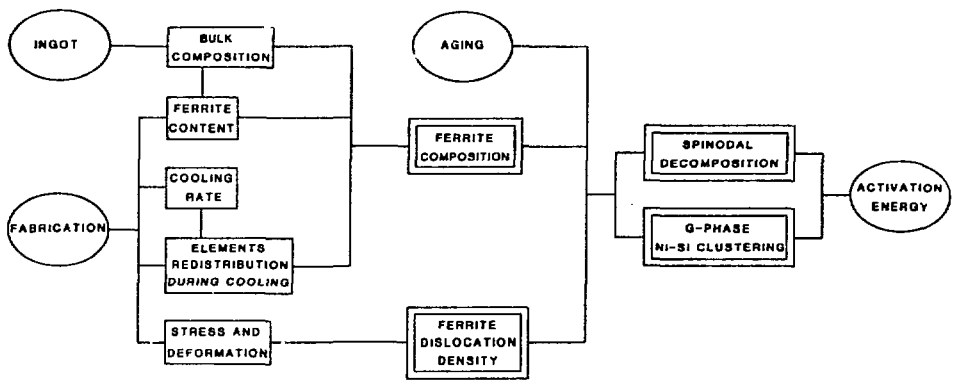

Fig. 10. Schematic Illustration of the Influence of Fabrication Process and Microstructural Evolution on the Activation Energy of Aging. Effects of $M_{23}C_6$ precipitation are not included.